TSINGHUA SCIENCE AND TECHNOLOGY
ISSN 1007-0214 07/11 pp199–207
DOI: 10.26599/TST.2019.9010058
Volume 26, Number 2, April 2021

Study of Texture Segmentation and Classification for Grading Small Hepatocellular Carcinoma Based on CT Images

Bei Hui*, Yanbo Liu, Jiajun Qiu, Likun Cao, Lin Ji, and Zhiqiang He

Abstract: To grade Small Hepatocellular CarCinoma (SHCC) using texture analysis of CT images, we retrospectively analysed 68 cases of Grade II (medium-differentiation) and 37 cases of Grades III and IV (high-differentiation). The grading scheme follows 4 stages: (1) training a Super Resolution Generative Adversarial Network (SRGAN) migration learning model on the Lung Nodule Analysis 2016 Dataset, and employing this model to reconstruct Super Resolution Images of the SHCC Dataset (SR-SHCC) images; (2) designing a texture clustering method based on Gray-Level Co-occurrence Matrix (GLCM) to segment tumour regions, which are Regions Of Interest (ROIs), from the original and SR-SHCC images, respectively; (3) extracting texture features on the ROIs; (4) performing statistical analysis and classifications. The segmentation achieved accuracies of 0.9049 and 0.8590 in the original SHCC images and the SR-SHCC images, respectively. The classification achived an accuracy of 0.838 and an Area Under the ROC Curve (AUC) of 0.84. The grading scheme can effectively reduce poor impacts on the texture analysis of SHCC ROIs. It may play a guiding role for physicians in early diagnoses of medium-differentiation and high-differentiation in SHCC.

Key words: grading of Small Hepatocellular CarCinoma (SHCC); Gray-Level Co-occurrence Matrix (GLCM); texture clustering; super-resolution reconstruction

1 Introduction

Hepatocellular CarCinoma (HCC) is a malignant tumor that originates in hepatic cells, which is the most common primary liver cancer and has a high mortality rate[1]. The pathological grade of an HCC reflects its degree of malignancy. Compared with high-differentiated HCCs, low-differentiated HCCs are more prone to spread, metastasize, and invade surrounding healthy tissue. To analyze and determine the prognosis of an HCC patient, it is important to accurately identify the pathological grade of the tumor. However, pathological differentiation of a tumor and its related immunohistochemistry can only be determined based on a pathology examination, which is necessarily invasive. However, invasive examinations cannot be performed in patients with surgical or puncture contraindications. Furthermore, pathological examinations are often time-consuming, which may reduce efficiencies and increase the risk of delaying therapies. Hence, the effective automated grading of tumor differentiation has great value to HCC patients.

In 2010, Huang and Lai[2] developed an automatic

• Bei Hui, Yanbo Liu, and Zhiqiang He are with the School of Information and Software Engineering, University of Electronic Science and Technology of China, Chengdu 610054, China. E-mail: bhui@uestc.edu.cn; 1264803611@qq.com; jianglinhe888@163.com.
• Jiajun Qiu is with the West China Biomedical Big Data Center, West China Hospital, Sichuan University, Chengdu 610041, China. E-mail: jiajun.ml@foxmail.com.
• Likun Cao is with the Department of Radiology of Peking Union Medical College Hospital, Beijing 100032, China. E-mail: clk2089@hotmail.com.
• Lin Ji is with the Department of Radiology, West China Hospital, Sichuan University, Chengdu 610041, China. E-mail: jilin2@sina.com.
* To whom correspondence should be addressed.
Manuscript received: 2019-09-29; revised: 2019-12-03; accepted: 2020-01-02

grading system for HCC biopsy images, used a watershed transformation method with control markers to obtain the initial contours of the nucleus, and a snake model to segment the nuclear shapes, and finally extracted 14 texture features and built an HCC-biopsy-image decision-graph classifier based on a Support Vector Machine (SVM). This classifier achieved 94.54% accuracy. In 2014, Atupelage et al.[3,4] developed an automated texture classification model to classify HCC grades based on the nuclear characteristics of the HCC cells, constructed two input pathways to separate the nuclear and non-nuclear structures of HCC, then extracted features of the HCC nuclei and built a random forest classifier, which achieved an accuracy of 95.97%. In 2018, Lin et al.[5] extracted texture features from 217 second-harmonic-generation microscope images using Gabor transformation, Haralick statistical analysis, and local binary patterns, and then built an SVM classifier to classify the HCC grades. However, the above studies all graded pathological images, which are obtained invasively. In this study, we graded HCC by extracting the texture features of CT images from early examinations, and then built a texture classification model by extracting the texture features of multiple layers by the texture analysis method. However, this method still presents some difficulties: (1) texture analysis is usually performed on a single CT image, which makes it difficult to comprehensively represent the textural characteristics inside a tumor; (2) in the study of small tumors, most HCC patients have small Regions Of Interest (ROIs), which makes it difficult to perform effective texture analysis; and (3) it is difficult to obtain ideal segmentation results for small-sample CT images of liver tumors, so fully automatic tumor segmentation remains challenging[6].

2 Materials and Data

A retrospective study was conducted on 105 cases of Small Hepatocellular CarCinoma (SHCC). These cases were selected from the West China Hospital of Sichuan University from January 2013 to present, for these SHCC cases were confirmed by pathological diagnoses after surgery. The differentiation grading of these SHCC cases follows the Edmondson-Steiner (E-S) grading criteria, where 68 cases are medium-differentiation SHCC (Grade II) and 37 cases are high-differentiation SHCC (Grades III and IV)[7]. In this study, we diagnosed medium-differentiation and high-differentiation SHCC, examples of which are shown in Fig. 1.

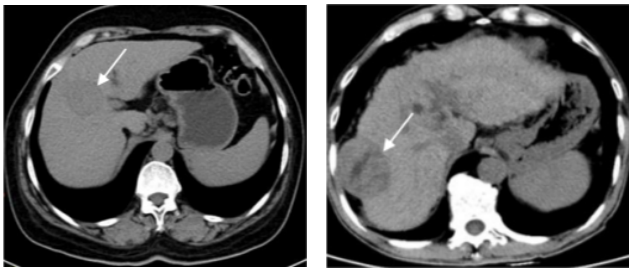

(a) (b)

Fig. 1 CT images of (a) medium-differentiation and (b) high-differentiation SHCC.

Nonenhanced CT images were used in the experiments. All slices were 512 pixel × 512 pixel. The images were acquired using a SIEMENS CT scanner (SOMATOM Definition AS+) with the following parameters: 120 – 140 kV, 210 mA, pitch 5 mm, window width 250 – 300 HU, window level 35 – 40 HU.

3 Experiment and Method

The grading scheme of this study comprises four stages: (1) training of a Super-Resolution Generative Adversarial Network (SRGAN) migration learning model on the LUng Nodule Analysis (LUNA) 2016 dataset and employing this pre-training model to reconstruct Super-Resolution (SR) images of the SHCC dataset (SR-SHCC images); (2) designing a texture clustering method based on a Gray-Level Co-occurrence Matrix (GLCM) to segment tumor regions from the original and SR-SHCC images as ROIs; (3) extracting the texture features of the ROIs; and (4) performing statistical analysis and classification. Figure 2 shows this scheme.

3.1 Super-resolution reconstruction of tumor regions

In recent years, machine-learning methods have made advances in the study of medical images[8,9]. The SRGAN is a method for performing super-resolution reconstruction using a Generative Adversarial Network (GAN) that can reconstruct a high-resolution image

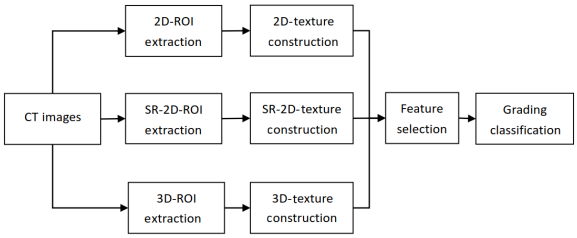

Fig. 2 Scheme used in this study.

from a single low-resolution image. The SRGAN uses a GAN to clarify the features of low-resolution images, then generates detailed information to supplement these low-resolution images, and finally creates high-quality reconstructed images. The SRGAN is built on a residual network (called SRResNet) and can improve the abstraction ability of convolutional networks and enable the reconstructed image to contain more high-frequency details. The SRGAN also defines perceptual loss and adversarial loss, which makes the generated and target images consistent in content and contour, as well as strongly similar in image style. This method ensures the realism of the reconstructed image and can also refine the texture details of a target while enlarging it[10,11].

This study was based on the LUNA 2016 dataset to pre-train an SRGAN migration learning model with 500 000 iterations. The LUNA dataset includes 1186 tumor data points from 888 patients. After loading the pre-trained data, the dataset was divided into a training set and a validation set at a ratio of 7:3 for migration learning with 200 000 iterations. The learning rate was set to 0.0001, the learning decay rate was set to 0.1, the maximum number of iterations was set to 200 000, and the conversion coefficient was 0.006.

In this paper, nonenhanced CT images of the 105 SHCC cases were input into the SRGAN model to obtain SR-SHCC images.

3.2 Tumor segmentation

The purpose of segmentation is to extract the tumor region, which is surrounded by normal liver tissue. With regard to the tumor texture, there are large number of invisible statistical rules, which can be used to reveal great differences between the two types of tissue. As such, these rules play an important role in tumor segmentation. For this study, we designed a GLCM-based texture clustering method to extract the texture features of a neighborhood, and then segment images at the pixel level.

3.2.1 Build GLCMs for each pixel

The textural differences between tumor regions and normal liver tissue can be effectively utilized for accurate and fully automatic tumor segmentation. If a neighborhood is too small (such as a 3 pixel×3 pixel neighborhood or a 5 pixel×5 pixel neighborhood), it is difficult to determine its texture. Therefore, in this study, we used 16 pixel×16 pixel neighborhood to construct the GLCMs.

3.2.2 Extract texture features from the GLCMs of each pixel

Five Haralick texture features (entropy, contrast, correlation, homogeneity, and energy) were utilized to indicate the texture differences between tumor regions and normal liver tissue.

3.2.3 Cluster the texture feature vectors

The texture features of a pixel comprise a texture feature vector. We used a K-means algorithm to cluster the texture feature vectors and calculated the weighted Euclidean distance to measure the similarity between two vectors. Equation (1) defines the distance (dist),

$$\mathrm{dist} = \sqrt{\sum_{k=1}^{n}\left(\frac{\boldsymbol{x}_{1k}-\boldsymbol{x}_{2k}}{S_k}\right)^2} \tag{1}$$

where $\boldsymbol{x}$ represents the feature vector, n represents the vector dimension, and S_k represents the standard deviation of the feature component. A abdominal CT image usually contains: (1) bone regions with higher gray values and simplex textures; (2) background regions with gray values close to 0 and almost no texture properties; (3) outer adipose layer regions with relatively invariable textures; (4) liver regions with clear textures; (5) other visceral regions with irregular textures; and (6) tumour regions that needed to be extract. Therefore, this study predefined 6 cluster centers and used these texture characteristics as prior knowledge, then performed cluster. The clustering results were first morphologically operated to connect the gaps generated in clustering and wipe off the extraneous scattered pixels, then formed texture clustering marks. The markers were mapped to the original CT image without any treatment, resulting in a post-marked image with true textures[12].

3.2.4 Extraction of tumor regions by a watershed immersion method

A tumor region can be extracted by performing a watershed immersion method on a CT image, which has texture clustering markers.

3.2.5 Obtaining ROIs

ROIs can be obtained in two steps: (1) calculating the longest path distance of a 2D tumor region based on the texture segmentation results, selecting the central point of the longest path across the 2D tumor region, and performing a morphological expansion operation to obtain a central rectangle inside the tumor region, until the point on the central rectangle is tangent to the tumor boundary (while ensuring that the upper point is tangent to the tumor boundary), such that the central rectangle

represents the 2D ROI of this tumor; (2) performing Step (1) on all tumor slices of a nonenhanced CT scan sequence and using the 2D ROIs to reconstruct a 3D ROI[13, 14]. Finally, a 2D ROI and a 3D ROI can be obtained from one case.

3.3 Multi-dimensional texture feature extraction

In this study, 2D and 3D texture features were extracted from original SHCC and SR-SHCC images.

3.3.1 2D-GLCM and SR-2D-GLCM features

In this paper, we describe the texture features based on a GLCM, which extracted 2D-GLCM features from the 2D ROIs in original SHCC CT images and SR-2D-GLCM features from 2D ROIs in SR-SHCC CT images. GLCMs are obtained by counting two pixels in an image with the same gray level in a distance and a direction[15]. Different statistical directions (0°, 45°, 90°, and 135°) can be selected to construct 2D-GLCMs. The five texture features, contrast, correlation, energy, homogeneity, and entropy, were extracted from the GLCMs[16].

3.3.2 Multi-scale 3D-GLCM features

Currently, 2D texture features are widely used in CT image analysis, but 2D textures can only describe the characteristics of a single CT image and cannot reflect the overall and internal texture changes of a tumor. In this study, we obtained a 3D ROI from a tumor, which inevitably contained abundant intratumoral texture information. In addition, in previous studies on 3D-GLCM features, a co-occurrence matrix has been established using a neighborhood model with a distance measure of "1", which only considers the correlation between the current voxel and a voxel value in the space "1" neighborhood in a certain direction. This kind of construction can only represent the spatial statistical law between the current CT image and its adjacent slices. However, in any combination of arbitrary directions and arbitrary distance measures, there may be a certain texture parameter that can more effectively distinguish two types of tissue regions[17, 18].

Therefore, we constructed a multi-scale 3D-GLCM using four distance measures, 1, 2, 3, and 4, to extract texture features called multi-scale 3D-GLCM features. Each voxel in a 3D tumor has 26 adjacent voxel blocks, so there are 26 spatial extension directions for a given voxel. According to the definition of a co-occurrence matrix, two co-occurrence matrices in two opposite directions from a line are completely identical. Therefore, we used 13 spatial directions to construct multi-scale 3D-GLCMs, for a total of 52 different 3D-GLCMs constructed. Figure 3 shows an example of the construction of a multi-scale 3D-GLCM. The distance measure is 1, which indicates a co-occurrence relationship between the current voxel and its surrounding 26 neighborhood voxels. However, the co-occurrence relationship exists only in adjacent slices (For example, i and j represent two adjacent voxels along the z axis direction in 3D space, as show in Fig. 3). If the distance measure is set to 2, the co-occurrence relationship can be extended to Slice 1, and the voxel-value-related characteristics of Slices 3 and 1 can be described. By selecting different distance measures and spatial directions, the statistical laws of the textures inside the 3D tumor can be more comprehensively represented, and the texture information can be utilized to a greater degree[19].

We extracted 12 texture features from the 3D-GLCM, including energy, entropy, correlation, contrast, homogeneity, variance, global average, moment of inertia of an area, clustering shadow, clustering significance, maximum probability estimation, and inverse difference moment.

3.4 Statistical analysis and classifications

Using the Mann-Whitney U test, we calculated the p-values of all the texture features in two types of samples, and selected all features with p-values less than 0.01 (defined as having significant differences) for subsequent classification experiments[20]. We used an SVM for classification (medium-differentiation and high-differentiation) and the leave-one-out method for model training. To evaluate the classification performance, we used seven indictors, including the Receiver Operating Characteristic (ROC) curve, Area Under the ROC

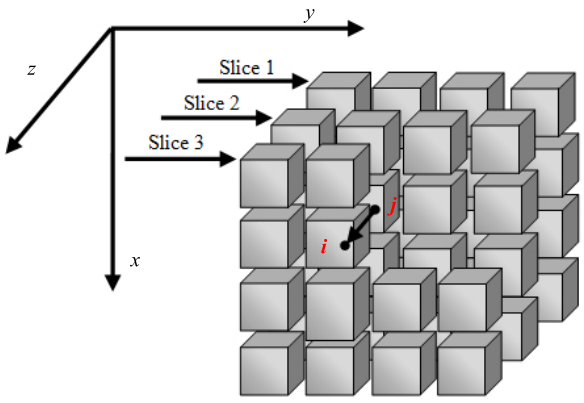

Fig. 3 Example of the construction of multi-scale 3D-GLCM.

Curve (AUC), ACCuracy (ACC), SENsitivity (SEN), SPEcificity (SPE), Positive Predictive Value (PPV), and Negative Predictive Value (NPV)[21].

4 Results and Discussion

Based on the trained SRGAN tumor migration learning model, an original SHCC CT image can be reconstructed to generate an SR-SHCC image with four times the resolution of the original image. Figures 4a and 4b show the SR-HCC and original SHCC images, respectively. From Fig. 4, we can see that the reconstructed HCC image has a larger lesion area than the original image and the textural details have high similarity to the original HCC lesion texture, thereby effectively solving the limitations associated with small ROIs in tumor segmentation, texture analysis, and classification. Moreover, the texture of the lesion and the quantitative analysis based on the texture features can play an auxiliary role in early diagnosis by physicians. An ROI that is too small will cause the extracted texture features to lack authenticity and comprehensiveness, which results in inaccurate experimental results, and makes it difficult to effectively perform texture-based segmentation and classification.

To compare our results with the super-resolution reconstruction method based on the SRGAN tumor migration model, we also performed bilinear interpolation[22,23] and bicubic interpolation[24] to reconstruct the super-resolution ROIs with details, shown in Figs. 5a and 5b, respectively. Figure 5c shows the part reconstructed using our proposed method, which is visually clearer and has more textural details, and image distortion can be prevented when magnifying the ROI.

To segment the tumor regions, i.e., the ROIs, we used the GLCM-based texture clustering method on the original and SR-SHCC images. Figure 6a shows an original HCC image, in which the tumor region is

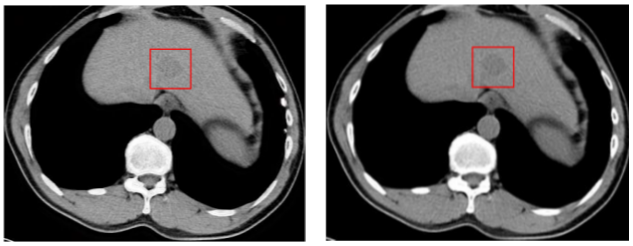

(a) (b)

Fig. 4 Example of super-resolution reconstruction. (a) Reconstructed super-resolution image and (b) an original image.

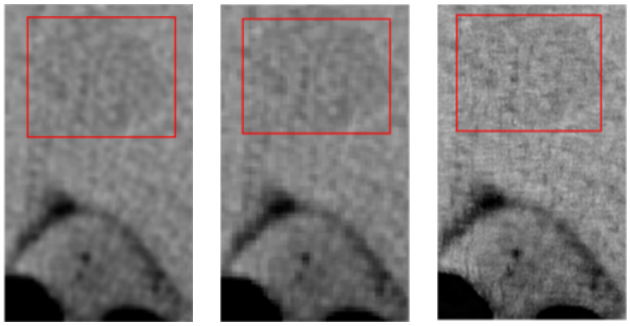

(a) (b) (c)

Fig. 5 Comparison of super-resolution reconstructions. (a) Bilinear interpolation, (b) bicubic interpolation, and (c) SRGAN migration learning model.

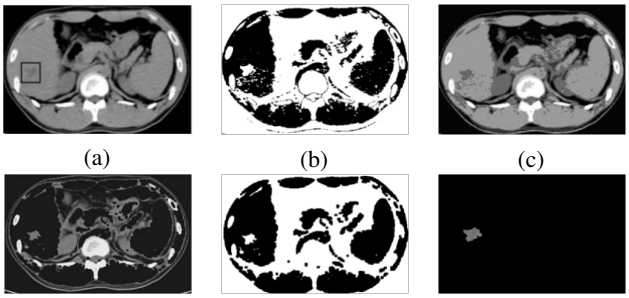

(a) (b) (c)

(d) (e) (f)

Fig. 6 Segmentation based on the GLCM texture clustering method. (a) Original image, (b) texture clustering result, (c) image after extraction of clustering markers, (d) result after morphological processing, (e) mapping of markers on the original image, and (f) tumor region.

encircled by a black wire frame, plaque-like shadows uneven in density, and slightly lower gradation than the surrounding region can be observed. Figure 6b shows the clustering result, from which it can be observed that the GLCM texture differences can be used to successfully distinguish the tumor region from normal liver tissue. Figure 6c shows the image after the extraction of the clustering markers. We removed the small holes that should not exist in the binary image by morphological operations, which generated the clustering marks shown in Fig. 6d. We then mapped the modified markers to the original image to obtain a tumor image with cluster markers, as shown in Fig. 6e, in which the tumor region is well distinguished from the surrounding normal liver tissue. Finally, we removed the connected regions and scatters smaller than 10 pixel×10 pixel in the marked image and processed it using the watershed immersion method to extract the whole tumor region, as shown in Fig. 6f.

Table 1 presents the segmentation performances of 10 cases that were randomly selected from the 105

Table 1 Accuracy comparison of segmentation algorithms.

CT scan	Original image			SR image		
	ACC	SEN	SPE	ACC	SEN	SPE
Patient 1	0.9472	0.9746	0.9315	0.8706	0.9238	0.8840
Patient 2	0.8507	0.8623	0.8243	0.8503	0.8865	0.8423
Patient 3	0.8949	0.9056	0.8746	0.8457	0.8326	0.8547
Patient 4	0.9091	0.9042	0.9166	0.8340	0.8876	0.8762
Patient 5	0.9376	0.9451	0.9023	0.7824	0.8023	0.8390
Patient 6	0.8995	0.9433	0.8842	0.9317	0.8951	0.8766
Patient 7	0.9029	0.9150	0.8827	0.8245	0.8329	0.7826
Patient 8	0.9058	0.8820	0.9152	0.8675	0.8464	0.8440
Patient 9	0.8819	0.8543	0.9476	0.9016	0.9451	0.8970
Patient 10	0.9201	0.9315	0.9018	0.8821	0.9016	0.8642
Mean	**0.9049**	**0.9117**	**0.8980**	**0.8590**	**0.8753**	**0.8560**

HCC cases. Using the manual segmentation results of senior physicians at the West China Hospital of Sichuan University as the gold standard, the GLCM-based texture clustering method achieved segmentation accuracies of 0.9049 and 0.8590 in the HCC original images and SR images, respectively. The segmentation performance of this algorithm for the SR image, however, is worse than that for the original image, which may be due to the noise generated by the super-resolution reconstruction and the loss of some texture information.

In this study, we extracted GLCM texture features from 2D ROIs, 3D ROIs, and SR-2D ROIs, which we refer to as 2D-GLCM features, 3D-GLCM features, and SR-2D GLCM features, respectively. Table 2 shows the results of the Mann-Whitney U test, which shows that for the SR-2D-GLCM features, the p-values of energy and entropy features (in the directions 0°, 45°, and 135°) are less than 0.01. The results of this study indicate that when the selected distance measure is too long, it is difficult to obtain a better classification effect, and the characteristics are not significantly different in the two types of SHCC.

In this study, there is no significant difference between the high- and medium-differentiation SHCC in contrast feature of image extracted based on SR-2D-GLCM method. This may be related to the fact that we used the lung tumor regions of CT images for the migration learning of the SRGAN, and these lung tumor regions had a higher overall brightnesses and lower contrast than the liver tumor regions of the CT images. Therefore, this feature is also reflected in the generated super-resolution images. However, the entropy and energy features show strong differences in the two types of SHCC, which has a better result than in the original images. In the original image, when the ROI is small, it is often difficult to fully obtain the internal texture statistics of small liver cancers with different levels of differentiation. Due to the reduction in the number of pixels, the texture differences are also more subtle, which makes it difficult to perform statistical and quantitative analyses. However, by preserving the original texture style, the reconstructed image increases the number of

Table 2 Results of the Mann-Whitney U test (including mean value and standard deviation).

Method	Feature	Mean± SD		p-value	Feature description
		Medium-differentiation SHCC	High-differentiation SHCC		
2D-GLCM	G1	8.0200±2.5300	9.6700±2.7800	0.0080	Contrast(0°)
	G2	5.9800±1.9600	6.9300±2.0500	0.0090	Contrast(0°)
SR-2D-GLCM	SR1	0.0360±0.0080	0.0320±0.0060	0.0030	SR-Energy(0°)
	SR2	5.2700±0.3000	5.4400±0.2700	0.0060	SR-Entropy(0°)
	SR3	0.0280±0.0060	0.0240±0.0040	0.0050	SR-Energy(45°)
	SR4	5.6600±0.2900	5.8200±0.2500	0.0080	SR-Entropy(45°)
	SR5	0.0270±0.0060	0.0240±0.0040	0.0050	SR-Energy(135°)
	SR6	5.6800±0.2900	5.8300±0.2400	0.0070	SR-Entropy(135°)
3D-GLCM	T1	0.9960±0.0030	0.9940±0.0040	0.0010	Homogeneity(1, [0 1 0])
	T2	0.0340±0.0100	0.0370±0.0100	0.0020	Contrast(1, [0 1 −1])
	T3	0.0510±0.0100	0.0560±0.0130	0.0080	Inertia(1, [−1 −1 −1])
	T4	0.0160±0.0100	0.0220±0.0100	0.0050	Entropy(1, [1 0 −1])
	T5	0.0600±0.0200	0.0800±0.0300	0.0030	Contrast(2, [1 −1 −1])
	T6	0.0170±0.0100	0.0200±0.0100	0.0060	Entropy(2, [−1 1 −1])
	T7	0.9500±0.0030	0.9300±0.0050	0.0030	Max probability(2, [−1 1 0])
	T8	0.0019±0.0010	0.0027±0.0040	0.0060	Inverse variance(2, [−1 0 0])
	T9	0.9000±0.0060	0.9800±0.0090	<0.0010	Energy(3, [0 0 −1])
	T10	0.0100±0.0110	0.0200±0.0160	<0.0010	Entropy(3, [1 1 −1])

pixels in the original ROI, and the textural laws are clearer and more comprehensive. This confirms that when the ROI in a complex image is small, the texture analysis of its super-resolution image may be better than that of the original image.

To perform classifications, we used an SVM classifier (polynomial kernel) and the leave-one-out method[25, 26]. Table 2 shows the three sets of features. We performed classifications based on each set of features, on two combined sets of features, and on three combined sets of features. Thus, seven classification experiments were performed, which are abbreviated as S1 – S7.

Table 3 shows the classification results of the single-set features (S1 – S3). The SR-2D-GLCM feature set yields the best experimental results, which indicates that the processing of the SR reconstruction significantly improved the experimental results. The experimental results of the 3D-GLCM features are better than those of the 2D-GLCM features, which demonstrates the advantages of 3D texture features in expressing the internal texture characteristics of tumors.

Table 4 shows the classifications of the combinations of two sets of features (S4 – S6) and three sets of features (S7), for which S7 achieved the best performance. The combination of the SR-2D-GLCM features, 2D-GLCM features, and 3D-GLCM features for the medium- and high-differentiation in SHCC yields a better result than using a single set of features.

The limitations of this study are as follows. (1) Being a single-center study, it was difficult to extend the results to other institutions; (2) Cross training and validation were performed to adjust the parameters of the model, but these were limited by the difficulty in obtaining grading results of the SHCC data, and we used no other subsets to further evaluate the generalizability of the model; (3) Because we were limited by the number of samples, this study lacked a test part, and may suffer from overfitting; (4) Because we extracted 18 features from 105 data, there may be some overfitting. In future studies, we will expand the sample size and test more methods.

In the past, gene sequencing has been used to identify and grade HCC or other types of cancer, and some positive research results have been achieved. Recently, this kind of research has again become a research hotspot. In subsequent work, on the one hand, we will focus on the relationship between PD-L1 expression level, patient genotype, and CT image features. On the other hand, we will also committed to finding new and fully automated methods for the diagnosis of small liver cancer and other liver cancers[27–30].

5 Conclusion

This paper presented the results of our radiomic study[31] on the grading of medium-differentiation and high-differentiation SHCC in nonenhanced CT images. The proposed scheme trained an SRGAN migration learning model on an LUNA dataset to perform SR reconstruction, designed a texture clustering method based on GLCM to extract tumor regions from original and SR images, then extracted multiple dimensional texture features and performed classifications. This proposed grading scheme can effectively reduce the poor impacts on the texture analysis of SHCC ROIs and may play a guiding role for physicians in the early diagnoses of medium-differentiation and high-differentiation in SHCC. The proposed scheme can also be extended to other types of differential diagnoses of liver lesions.

Acknowledgment

This work was supported by the National Key R&D Program of China (No. 2018YFC0807500).

Table 3 Performance comparison of single set features.

Set	Method	ACC (%)	SEN (%)	SPE (%)	PPV (%)	NPV (%)	AUC
S1	2D-GLCM	65.71	72.05 (49/68)	54.05 (20/37)	74.24	51.28	0.64
S2	**SR-2D-GLCM**	**78.09**	**85.29 (58/68)**	**64.86 (24/37)**	**81.69**	**70.58**	**0.80**
S3	3D-GLCM	74.28	77.94 (53/68)	67.56 (25/37)	81.53	62.50	0.75

Table 4 Performances comparison of texture classification models.

Set	Method	ACC (%)	SEN (%)	SPE (%)	PPV (%)	NPV (%)	AUC
S4	SR-2D-GLCM&2D-GLCM	80.95	86.76 (59/68)	70.27 (26/37)	84.28	74.28	0.82
S5	2D-GLCM&3D-GLCM	78.09	80.88 (55/68)	72.97 (27/37)	84.61	67.50	0.79
S6	SR-2D-GLCM&3D-GLCM	80.00	77.94 (53/68)	83.78 (31/37)	89.83	67.39	0.83
S7	**ALL**	**83.80**	**88.23 (60/68)**	**75.67 (28/37)**	**86.95**	**77.77**	**0.84**

References

[1] P. Bertuccio, F. Turati, G. Carioli, T. Rodriguez, C. Lavecchia, M. Malvezzi, and E. Negri, Global trends and predictions in hepatocellular carcinoma mortality, *Journal of Hepatology*, vol. 67, no. 2, pp. 302–309, 2017.

[2] P. Huang and Y. Lai, Effective segmentation and classification for HCC biopsy images, *Pattern Recognition*, vol. 43, no. 4, pp. 1550–1563, 2010.

[3] C. Atupelage, H. Nagahashi, F. Kimura, M. Yamaguchi, T. Abe, A. Hashiguchi, and M. Sakamoto, Computational cell classification methodology for hepatocellular carcinoma, in *Proc. of International Conference on Advances in ICT for Emerging Regions*, Bauddhaloka Mawatha, Sri Lanka, pp. 21–27, 2013.

[4] C. Atupelage, H. Nagahashi, M. Yamaguchi, T. Abe, A. Hashiguchi, and M. Sakamoto, Multifractal feature descriptor for grading hepatocellular carcinoma, presented at the 23rd Annu. Meeting International Conference on Pattern Recognition, Amsterdam, the Netherlands, 2016.

[5] H. Lin, L. Lin, G. Wang, N. Zuo, Z. Zhan, S. Xie, G. Chen, J. Chen, and S. Zhou, Label-free classification of hepatocellular-carcinoma grading using second harmonic generation microscopy, *Biomedical Optics Express*, vol. 9, no. 8, pp. 3783–3797, 2018.

[6] A. H. Mir, M. Hanmandlu, and S. N. Tandon, Texture analysis of CT images, *IEEE Engineering in Medicine and Biology Magazine*, vol. 14, no. 6, pp. 781–786, 1995.

[7] Chinese Society of Liver Cancer, Chinese Anti-Cancer Association, Liver Cancer Study Group, Chinese Society of Hepatology, Chinese Medical Association, and Chinese Society of Pathology, Evidence-based practice guidelines for the standardized pathological diagnosis of primary liver cancer in China (2015 update), *Journal of Clinical Hepatology*, vol. 23, no. 5, pp. 321–327, 2015.

[8] J. Liu, Y. Pan, M. Li, Z. Chen, L. Tang, C. Lu, and J. X. Wang, Applications of deep learning to MRI images: A survey, *Big Data Mining and Analytics*, vol. 1, no. 1, pp. 1–18, 2018.

[9] J. Lötsch, F. Lerch, R. Djaldetti, I. Tegder, and A. Ultsch, Identification of disease-distinct complex biomarker patterns by means of unsupervised machine-learning using an interactive R toolbox (Umatrix), *Big Data Analytics*, vol. 3, no. 1, p. 5, 2018.

[10] J. Qiao, H. Song, and K. Zhang, Image super-resolution using conditional generative adversarial network, *IET Image Processing*, vol. 13, no. 4, pp. 2673–2677, 2019.

[11] C. Ledig, L. Theis, F. Huszar, J. Caballero, A. Cunningham, A. Acosta, A. Aitken, A. Tejani, J. Totz, and Z. Wang, Photo-realistic single image super-resolution using a generative adversarial network, *Computer Vision & Pattern Recognition*, doi:10.1109/CVPR.2017.19.

[12] D. A. Clausi, K-means Iterative Fisher (KIF) unsupervised clustering algorithm applied to image texture segmentation, *Pattern Recognition*, vol. 35, no. 9, pp. 1959–1972, 2002.

[13] B. Yu, L. Yan, and F. Chao, An improved watershed segmentation method of medical image, *Applied Mechanics and Materials,* vols. 719&720, no. 3, pp. 1009–1012, 2015.

[14] J. Chen and S. Liu, A medical image segmentation method based on watershed transform, presented at the 5th Annu. Meeting International Conference on Computer & Information Technology, Shanghai, China, 2005.

[15] R. M. Haralick, K. Shanmugam, and I. H. Dinstein, Textural features for image classification, *IEEE Transactions on Systems, Man & Cybernetics*, vol. 3, no. 6, pp. 610–621, 1973.

[16] W. Zhou, L. Zhang, K. Wang, S. Chen, G. Wang, Z. Liu, and C. Liang, Malignancy characterization of hepatocellular carcinomas based on texture analysis of contrast-enhanced MR images, *Journal of Magnetic Resonance Imaging,* vol. 45, no. 5, pp. 1476–1484, 2016.

[17] D. Mahmoud-Ghoneim, G. Toussaint, J. Constans, and J. D. de Carteines, Three dimensional texture analysisin MRI: Preliminary evaluation in gliomas, *Magnetic Resonance Imaging*, vol. 21, no. 9, pp. 983–987, 2003.

[18] M. S. M. Rahim, T. Saba, F. Nayer, and A. Z. Syed, 3D texture features mining for MRI brain tumor identification, *3D Research,*, vol. 5, no. 3, pp. 1–8, 2014.

[19] T. Y. Kim, N. H. Cho, G. B. Jeong, E. Bengtsson, and H. K. Choi, 3D texture analysis in renal cell carcinoma tissue image grading, *Computational and Mathematical Methods in Medicine,* vol. 2014, pp. 1–12, 2014.

[20] D. W. Zimmerman, Comparative power of student T test and Mann-Whitney U Test for unequal sample sizes and variances, *Journal of Experimental Education*, vol. 55, no. 3, pp. 171–174, 2014.

[21] M. H. Horng, Performance evaluation of multiple classification of the ultrasonic supraspinatus images by using ML, RBFNN, and SVM classifiers, *Expert System with Application*, vol. 37, no. 41, pp. 46–55, 2010.

[22] K. T. Gribbon and D. G. Bailey, A novel approach to real-time bilinear interpolation, *IEEE International Workshop on Electronic Design*, doi: 10.1109/DELTA.2004.10055.

[23] J. Lu, X. Si, and S. Wu, An improved bilinear interpolation algorithm of converting standard-definition television images to high-definition television images, presented at the 2nd Annu. Meeting WASE International Conference on Information Engineering, Taiyuan, China, 2009.

[24] X. Zhao, S. Yun, Y. Dong, J. WANG, and L. Zhai, Kind of super-resolution method of CCD image based on wavelet and bicubic interpolation, *Application Research of Computers*, vol. 26, no. 6, pp. 2365–2367, 2009.

[25] D. Feng, F. Chen, and W. Xu, Efficient leave-one-out strategy for supervised feature selection, *Tsinghua Science and Technology*, vol. 18, no. 6, pp. 629–635, 2013.

[26] P. Phoungphol, Y. Zhang, and Y. Zhao, Robust multiclass classification for learning from imbalanced biomedical data, *Tsinghua Science and Technology*, vol. 17, no. 6, pp. 619–628, 2012.

[27] Z. Cai, R. Goebel, M. R. Salavatipour, and G. Lin, Selecting dissimilar genes for multi-class classification, an application in cancer subtyping, *BioMed Central Bioinformatics*, vol. 8, no. 1, p. 206, 2007.

[28] Z. Cai, M. Heydari, and G. Lin, Clustering binary Oligonucleotide fingerprint vectors for DNA clone classification analysis, *Journal of Combinatorial Optimization*, vol. 9, no. 2, pp. 199–211, 2005.

[29] K. Yang, Z. Cai, J. Li, and G. Li, A stable gene selection in microarray data analysis, *BioMed Central Bioinformatics*, vol. 7, no. 1, p. 228, 2006.

[30] Z. Cai, T. Zhang, and X. Wan, A computational framework for influenza antigenic cartography, *PLoS Computational Biology*, vol. 6, no. 10, pp. 1–14, 2010.

[31] R. J. Gillies, P. E. Kinahan, and H. Hricak, Radiomics: Images are more than pictures, they are data, *Radiology*, vol. 278, no. 2, pp. 563–577, 2016.

Bei Hui received the PhD degree from the University of Electronic Science and Technology of China (UESTC) in 2009. He is now an associate professor at the School of Information and Software Engineering, University of Electronic Science and Technology of China. His research interests include machine learning and medical image processing.

Yanbo Liu is currently a master student at University of Electronic Science and Technology of China. His research interests include texture analysis, machine learning, and medical image processing.

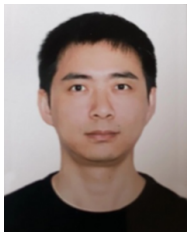

Jiajun Qiu received the PhD degree from the University of Electronic Science and Technology of China in 2019. He is a data scientist of West China Biomedical Big Data Center, Sichuan University. His research interests include radiomics and machine learning.

Likun Cao received the master degree from Sichuan University in 2019. She is now a radiologist of Peking Union Medical College Hospital. Her research interests include radiology and computer-aided diagnosis.

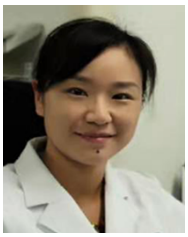

Lin Ji received the PhD degree from Sichuan University in 2014. She is a radiologist of the West China Hospital, Sichuan University. Her research interests include radiology and computer-aided diagnosis.

Zhiqiang He is a master student at the School of Information and Software Engineering, University of Electronic Science and Technology of China. His research interests include machine learning and medical image processing.